

Core pinning by intragranular nanoprecipitates in polycrystalline MgCNi₃

L. D. Cooley, X. Song, J. Jiang, and D. C. Larbalestier*

Applied Superconductivity Center, University of Wisconsin, Madison, Wisconsin 53706

T. He, K. A. Regan, and R. J. Cava

Department of Chemistry and Princeton Materials Institute, Princeton University, Princeton, New Jersey 08544

(Received 8 March 2002; published 4 June 2002)

The magnetic properties and nanostructure of polycrystalline MgCNi₃, prepared from a batch with overall composition MgC_{1.5}Ni₃, were studied by vibrating sample magnetometry and electron microscopy. Very high critical current density, e.g., 1.8 MA/cm² at 1 T and 4.2 K, is deduced from the magnetic hysteresis and evident subdivision of the sample into 10 μm clusters of MgCNi₃ grains by excess graphite. The bulk pinning force $F_p(H)$ is comparable to that of other strong flux-pinning superconductors, such as NbN, Nb-Ti, and Nb₃Sn, all of which have higher critical temperatures. While $F_p(H)$ indicates the expected grain-boundary pinning mechanism just below $T_c \approx 7.2$ K, a systematic change to a core-pinning mechanism is indicated by a shift of the $F_p(H)$ curve peak to higher (reduced) field with decreasing temperature. The lack of temperature scaling of $F_p(H)$ suggests the presence of pinning sites at a nanometer scale inside the grains, which are smaller than the diameter of fluxon cores $2\xi(T)$ at high temperature and become effective when the coherence length $\xi(T)$ approaches the nanostructural scale with decreasing temperature. High-resolution transmission electron microscopy imaging and electron diffraction revealed a substantial volume fraction of cubic and graphite nanoprecipitates comparable to $\xi(0) \approx 5$ nm in size, consistent with the hypothesis above. Dirty-limit behavior seen in previous studies may thus be tied to electron scattering by the precipitates. To our knowledge, no other fine-grained bulk intermetallic superconductor exhibits a similar change from grain boundary to core pinning with decreasing temperature, suggesting that the arrangement of pinning sites in MgCNi₃ is unique. These results also indicate that strong flux pinning might be combined with a technologically useful upper critical field if variants of MgCNi₃ with higher T_c can be found.

DOI: 10.1103/PhysRevB.65.214518

PACS number(s): 74.60.Ge, 74.20.Mn

I. INTRODUCTION

The recent discovery¹ of superconductivity above 7 K in MgCNi₃ suggests the possibility of a new family of nickel-carbide superconductors. MgCNi₃ is related both structurally and chemically to the layered RNi₂B₂C compounds (R =rare earth or Y), which exhibit superconductivity up to 17 K for LuNi₂B₂C.² In particular, the three-dimensional cubic arrangement of Ni atoms in MgCNi₃ is related to the two-dimensional square-planar arrangement of Ni in the RNi₂B₂C family. It has been proposed that, in analogy to copper and bismuth-oxide perovskites, the conduction in MgCNi₃ involves holes in the Ni d states.¹ Such holes are usually responsible for magnetism rather than superconductivity. The possibility, therefore, of unconventional superconductivity has attracted great interest in the band structure and the physics of the pairing mechanism.^{3–6} From an application point of view, it is interesting that MgCNi₃ behaves like a dirty-limit intermetallic superconductor, with a high resistivity and a steep slope of the upper critical field H_{c2} at the critical temperature T_c .⁷ This produces $\mu_0 H_{c2}(0)$ values of 15 T,⁷ comparable to the reported 8–15 T values for the layered, clean-limit borocarbide compounds⁸ that have 2–3 times higher T_c .

In this article, we present evidence for nanometer-scale precipitation in MgCNi₃, which may explain why dirty-limit behavior is observed. Bulk pinning-force curves $F_p(H)$ derived from magnetization data show a systematic change with decreasing temperature, from behavior characteristic of

grain-boundary pinning near $T_c \approx 7.2$ K to behavior characteristic of core pinning at 1.8 K. This implies the existence of intragranular pinning sites that are invisible to flux lines at high temperature, when the flux-line diameter 2ξ is large, but become effective at low temperature, when $\xi(T)$ is slightly larger than $\xi(0) \approx 5$ nm. Evidence for both graphite precipitates and an unidentified phase with cubic symmetry is provided by high-resolution transmission electron microscopy (TEM). Both precipitates have 5 nm size, as deduced from moiré fringe patterns. These nanoprecipitates probably result from the processing of MgCNi₃, since excess carbon is needed to get the highest values of T_c .¹ We are drawn to the interesting conclusion that MgCNi₃ may be unique among high-field intermetallic superconductors, since it can be made with intragranular core-pinning sites that are necessary for strong pinning at high fields, a feature not found in, e.g., Nb₃Sn, Nb₃Ge, or NbN. Ni-based intermetallic superconductors might therefore be interesting for high-field magnet applications if new compounds with higher T_c can be found.

II. EXPERIMENT

A MgCNi₃ pellet from a batch reported in Ref. 1 was studied, with nominal formula MgC_{1.5}Ni₃. Light microscopy of polished pieces cut from the pellet showed a dense, shiny phase with <5% porosity. Small regions of pure carbon (as graphite) were visible and indicated by x-ray analyses. Scanning and transmission electron microscopy, Fig. 1, show that

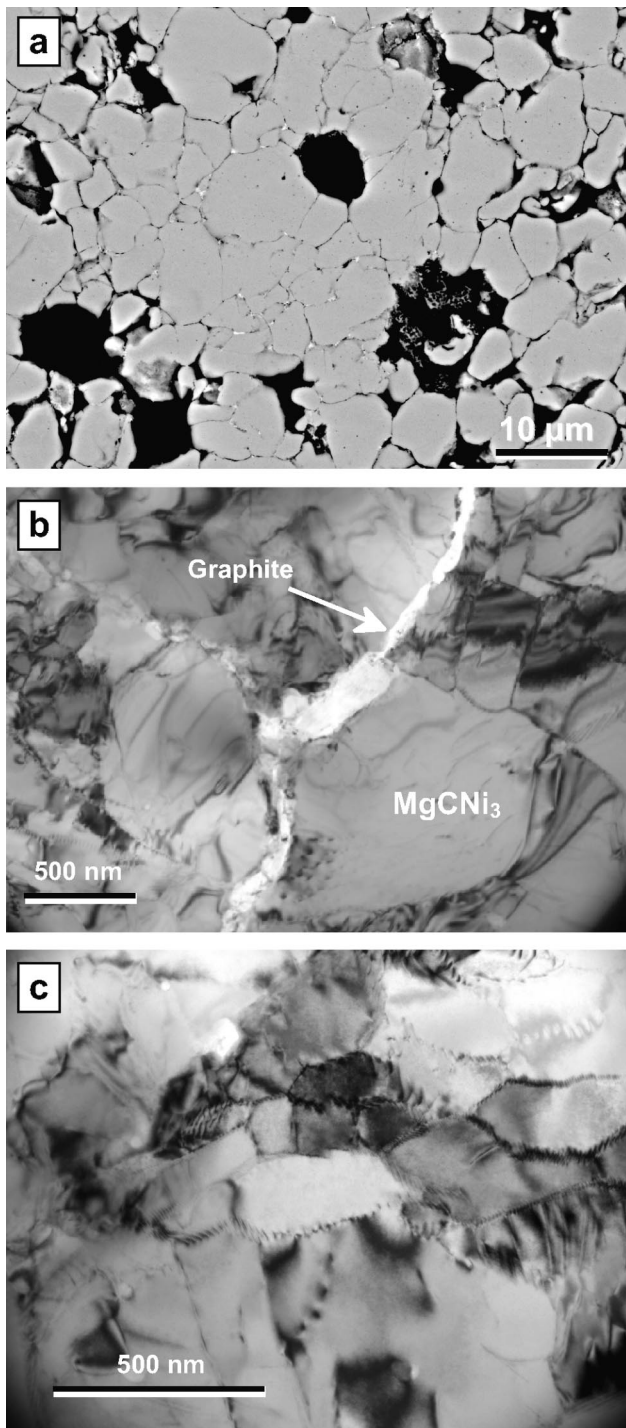


FIG. 1. Electron micrographs of a polished sample. (a) MgCNi_3 colonies appear as light gray regions about $10\ \mu\text{m}$ in size when examined by scanning electron microscopy, with excess graphite appearing as the black regions in between colonies. (b) Transmission electron micrograph shows that the MgCNi_3 colonies are separated by a graphite layer. (c) Within each colony, MgCNi_3 grains are $100\text{--}300\ \text{nm}$ in size. The appearance of grain-boundary dislocations suggests low angles of misorientation between some grains.

the samples consist of random polycrystal colonies of MgCNi_3 ranging from 1 to $10\ \mu\text{m}$ in size. Thin regions of carbon in the boundaries between colonies were common. TEM analyses at higher magnification reveal a finer grain

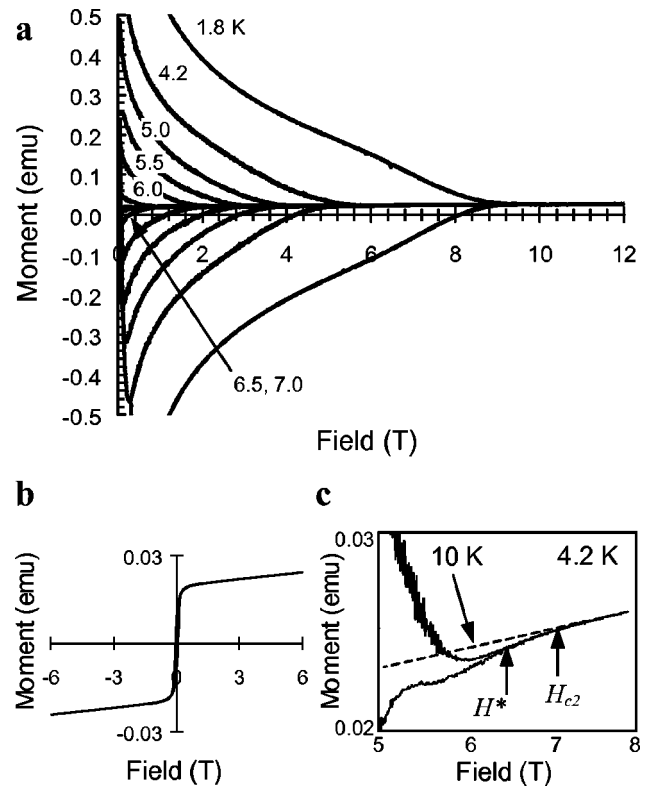


FIG. 2. (a) Magnetization curves from 1.8 to $7\ \text{K}$. (b) $10\ \text{K}$ data, showing a weak ferromagnetic background. The saturation magnetization is equivalent to the calculated moment of $0.5\ \text{vol.}\%$ pure Ni. (c) Magnified view of the magnetization loop closure at $4.2\ \text{K}$, showing how values for H^* and H_{c2} were determined.

structure inside each polycrystal colony, with size $100\text{--}300\ \text{nm}$. This grain size is typical of a polycrystalline intermetallic compound. Grain-boundary dislocations were evident along many grain boundaries, suggesting that a substantial number of grains have low angles of misorientation to each other within each colony.

Electromagnetic characterization was performed on a $3\ \text{mm}\times 3\ \text{mm}\times 0.5\ \text{mm}$ prism, which was later thinned for the TEM analyses described above and in more detail later. A vibrating sample magnetometer (VSM) was used to measure the sample moment $m(H, T)$ from 1.8 to $330\ \text{K}$ and in a field H from 0 to $14\ \text{T}$. In the superconducting state, raw hysteresis loops for 1.8 to $7.0\ \text{K}$, shown in Fig. 2(a), generally were symmetric around a weakly ferromagnetic background measured at $10\ \text{K}$, shown in Fig. 2(b). A slight bulge is evident at high field for the $1.8\ \text{K}$ curve, whereas curves taken at higher temperatures do not have this feature. The hysteresis loops actually close slightly below the field at which the background magnetization of the normal state is reached, at the irreversibility field $H^*(T)$, as shown in Fig. 2(c). A small, reversible diamagnetic magnetic moment (relative to the $10\ \text{K}$ background) was visible above H^* , which changed slope to overlap the $10\ \text{K}$ curve at the upper critical field $H_{c2}(T)$. The uncertainty in $\mu_0 H^*(T)$ is about $0.1\ \text{T}$, while that in $\mu_0 H_{c2}(T)$ is about $0.3\ \text{T}$.

The saturation magnetization M_{sat} at $10\ \text{K}$ is equivalent to the presence of 0.5% by volume of pure Ni impurities. By

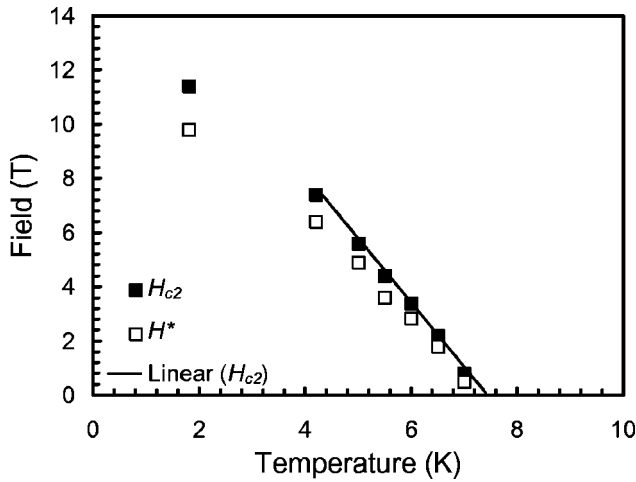


FIG. 3. Plot of the temperature dependence of the upper critical field and the irreversibility field. The line drawn through the $H_{c2}(T)$ data is a least-squares linear fit.

measuring $M_{sat}(T)$ at ~ 50 K intervals, a magnetic transition temperature T_m of 390 K and a scaling of $M_{sat}(T) \propto (T_m - T)^{0.078}$ were determined. However, these values are significantly different from established values for pure nickel, $T_m = 627.4$ K and an exponent of 0.378.⁹ Since such a low level of Ni is difficult to quantitatively determine by x-ray diffraction (XRD) or microscopy, further study is needed to understand the ferromagnetic behavior.

The critical-field-temperature results, shown in Fig. 3, are similar to the recent results of Li *et al.*⁷ Based on a linear fit of the 4.2–7 K data, we find a slope $\mu_0 dH_{c2}/dT$ of -2.3 T/K at T_c , which yields an extrapolated upper critical field at zero temperature, $\mu_0 H_{c2}(0) = 0.69 T_c dH_{c2}/dT$, of about 11.4 T using the T_c reported in Ref. 1 (7.2 K). Due to the fact that the inductive transitions were not sharp,¹ a better estimate of $\mu_0 H_{c2}(0)$ is 12.8 T, which includes our measured 11.4 T value at 1.8 K. This value for $\mu_0 H_{c2}(0)$ is close to that reported in Ref. 7, 15 T. Based on our extrapolated $H_{c2}(0)$ value, the coherence length at 0 K, $\xi(0)$

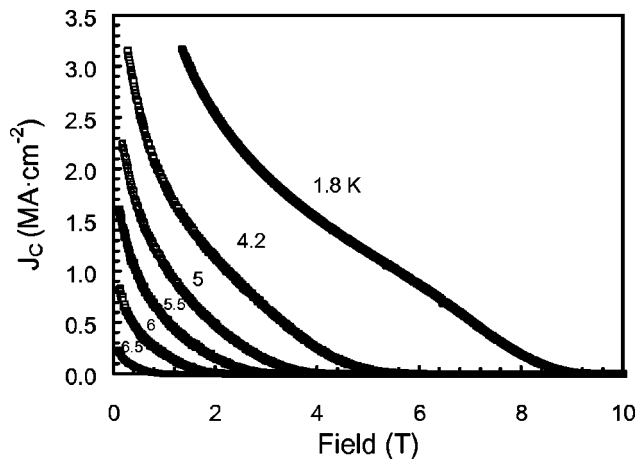


FIG. 4. Critical current density at 1.8–6.5 K, assuming magnetization current loops flow around grain colonies with diameter 10 μm .

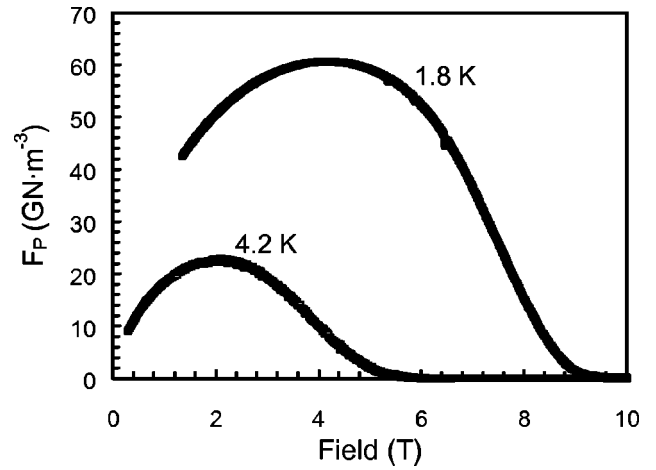


FIG. 5. Bulk pinning force at 1.8 and 4.2 K derived from the $J_c(H)$ data, using a scaling length equal to the 10 μm colony size.

$= (2\pi\mu_0 H_{c2})^{1/2}$, is 5.0 nm. The difference between the irreversibility field, also shown in Fig. 3, and the upper critical field at 4.2 K is about 1 T, which is similar to that found in Nb 48 wt % Ti and less than that of Nb₃Sn at 4.2 K.¹⁰

The critical current density $J_c(H, T)$ was determined by applying standard critical-state expressions to the magnetization data.¹¹ Assuming the current flows around the entire sample, the critical state of a thin square prism in perpendicular field applies, giving $J_c = 3\Delta M/d$, where ΔM is the full width of the magnetization hysteresis and $d = 3$ mm is the width of the sample (SI units). From this evaluation, J_c is about 10^3 – 10^4 A/cm² at 4.2 K. However, since the microstructural analyses (Fig. 1) show carbon between grain colonies, a more appropriate expression is the critical state of a sphere with diameter $2a \approx 10$ μm , giving $J_c = 16\Delta M/3\pi a \approx 1.8 \times 10^6$ A/cm² at 1 T, 4.2 K. $J_c(H)$ data are shown in Fig. 4. The bulk pinning force $F_p(H) = \mu_0 H \times J_c(H, T)$ derived from the $J_c(H)$ data, shown in Fig. 5, reaches very high values under the latter assumption. For instance, the peak value at 4.2 K, 23.5 GN/m³, is higher than that of optimized Nb 48 wt % Ti (Ref. 12) at 4.2 K even though Nb 48 wt % Ti has a slightly higher irreversibility field at that temperature ($\mu_0 H^* \approx 10$ T).

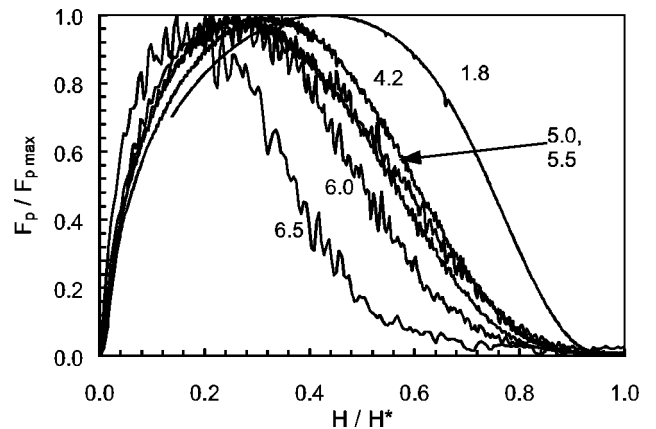


FIG. 6. Reduced bulk pinning-force curves at 1.8–6.5 K. Note that curves for 5.0 and 5.5 K nearly overlap.

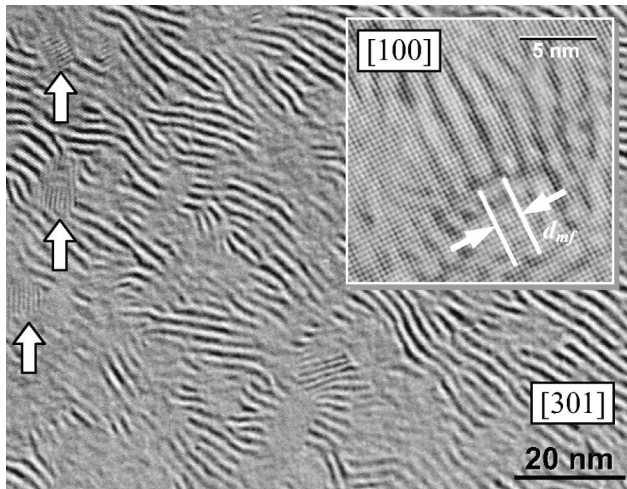


FIG. 7. High-resolution TEM images from a thin region of the sample, taken along the $[301]$ zone axis. Arrows indicate moiré fringe domains caused by precipitates that are not aligned with the zone axis. Inset: high-resolution image taken along the $[100]$ zone axis showing moiré fringe spacing relative to atomic rows of the MgCNi_3 phase. The lattice fringe separation spans approximately five MgCNi_3 unit cells.

III. DISCUSSION

In conventional superconductors, the flux-pinning mechanism associated with microstructural defects is often assessed by analyzing the shape of $F_p(H)$ as a function of temperature. Reduced curves $F_p(h, T)/F_{p\max}(h, T)$ plotted against a normalized field $h = H/H^*(T)$ typically overlap when a single pinning mechanism and pinning center is dominant,¹³ and this behavior would be expected if, e.g., grain boundaries alone were the pinning centers. Such scaling behavior is commonly observed in intermetallic low-temperature superconductors such as Nb_3Sn .^{14–16} By contrast, a constant shape of the bulk pinning-force curve is not obeyed as a function of temperature in the present experiment, as shown in Fig. 6. Instead, a systematic shift of the reduced pinning-force curve peak toward higher field occurs as the temperature is reduced. This behavior strongly suggests that different pinning mechanisms and pinning centers are at work for temperatures near to and far below T_c , respectively.

The nanostructural analyses in Fig. 1 suggest that grain boundaries within each polycrystalline colony and the carbon layers that separate colonies are two possible pinning centers. However, due to the large size of the colonies compared to the flux-line separation at high field, the carbon layers probably act as a surface barrier and contribute little to the overall pinning force above about 0.5 T.¹⁷ It is also very unlikely that pinning by grain boundaries is the dominant pinning mechanism at 1.8 K, because the observed grain size of 100–300 nm is comparable to that seen in widely studied Nb_3Sn composites, for which the peak of $F_p(H)$ is rarely higher than $h = 0.25$.¹⁵ Instead, the 1.8 K curve has the shape expected for core pinning by voids or precipitates at scales smaller than the resolution of Fig. 1.^{12,18} On the other hand,

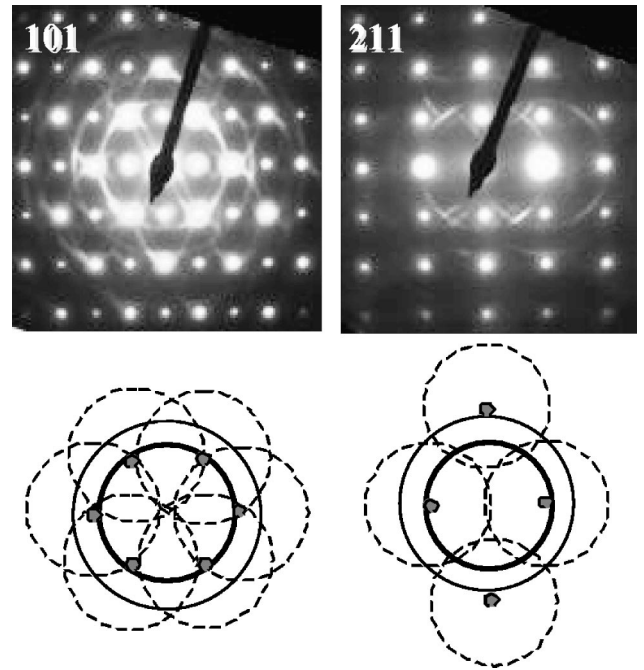


FIG. 8. Selected area diffraction patterns from the $[101]$ and $[211]$ zone axes, respectively. Arcs centered around the central electron beam (solid lines in the sketches below) are due to primary diffraction of graphite. Arcs centered around MgCNi_3 diffraction spots (dashed lines in the sketches) are due to double diffraction.

a grain-boundary pinning mechanism is consistent with the 6.5 K curve in Fig. 6.

The presence of a nanoscale system of pinning centers is revealed by high-resolution TEM imaging. Moiré fringes dominate high-resolution images taken from the thinnest regions of the TEM sample, as shown in Fig. 7. Since moiré fringes result when an electron beam transmitted through the main MgCNi_3 phase passes through another lattice with different atomic spacing,¹⁹ the high-resolution images suggest that either impurities are present on the sample surface or small precipitates are embedded within the MgCNi_3 matrix. However, the ion-milling process used to prepare the TEM specimens makes the first possibility unlikely, so we are led to conclude that moiré fringes are caused by precipitates.

Further, since domains in the fringe patterns correspond to the projected cross section of individual precipitates, the precipitate quantity and dimensions can be inferred from the high-resolution images. For instance, many domains appear in Fig. 7 taken along the $[301]$ MgCNi_3 zone axis, indicating a substantial volume fraction of precipitates. A large number of these domains have fringes that run generally from the upper left to the lower right of the main image, indicating that many precipitates share a common orientation with the selected MgCNi_3 zone axis (as discussed further later). Several of these domains appear to overlap, making it difficult to estimate the precipitate size. However, a few domains, indicated by arrows, show fringe patterns that run along the image vertical, due to larger misalignment of some precipitates with the zone axis. The size of the domains, about 5 nm, gives the approximate dimensions of the precipitates.

Selected-area diffraction patterns were acquired to iden-

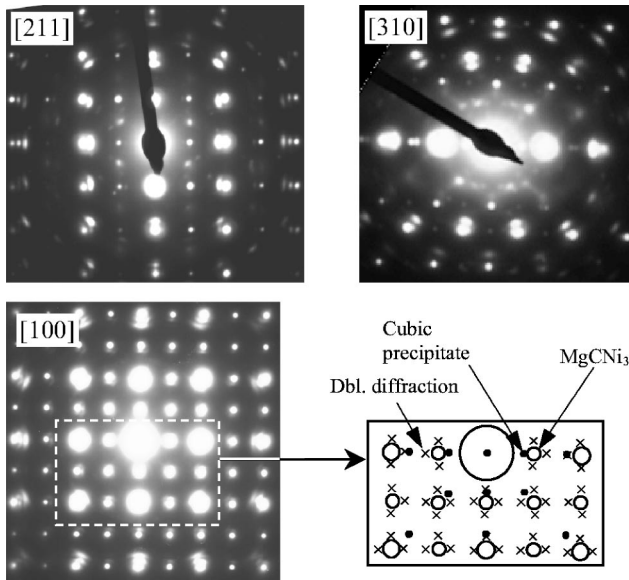


FIG. 9. Selected area diffraction patterns from the $[2\bar{1}1]$, $[301]$, and $[100]$ MgCNi_3 zone axes. The sketch indicates primary diffraction spots from MgCNi_3 (\circ) and the cubic precipitate (\bullet), such as the (100) spots identified by arrows. Double-diffraction spots are also indicated (\times), for which primary diffraction beams from MgCNi_3 serves as incident beams for the precipitate. These double-diffraction spots are blurred by the overlapping primary spots.

tify the precipitate structure. Figure 8 shows selected-area diffraction patterns indicating graphite nanoprecipitates. The rectangular array of spots is produced by the MgCNi_3 for the indicated zone axes. Graphite is indicated by the weak arcs centered around the incident electron beam, where the arcs from the (101) and (015) planes (spacings of 0.208 nm and 0.146 nm, respectively) are brightest. Double diffraction produces arcs centered around the parent MgCNi_3 diffraction spots. The appearance of arcs rather than complete rings indicates that the graphite has some texture with respect to the MgCNi_3 lattice.

In addition to graphite nanoprecipitates, a second precipitate with cubic symmetry was identified. Diffraction patterns taken from various zone axes of the MgCNi_3 phase, shown in Fig. 9, have weaker secondary spots in addition to the primary spots from MgCNi_3 . Some of the secondary spots can be indexed as primary diffraction from a cubic phase with larger lattice parameter, while the others can be attributed to double diffraction. For example, the diffraction pattern along the MgCNi_3 $[100]$ zone axis and its corresponding indexing are shown in Fig. 9. In view of the diffraction pattern in Fig. 9 and those taken from several other zone axes, a lattice parameter of 0.47 nm can be determined for the cubic precipitate if the lattice parameter of MgCNi_3 , $d_0 = 0.381$ nm,¹ is used as the reference. As a cross-check, it is interesting that the moiré fringe spacing along the $[100]$ zone axis d_{mf} is 1.96 nm, as indicated in Fig. 7, inset. From this spacing, a lattice parameter $d_1 = 0.47$ nm can be obtained using the reciprocal relationship $d_{\text{mf}} = d_0 d_1 (d_1 - d_0)^{-1}$. This lattice parameter agrees with the value obtained from diffraction above. When considered together, the diffraction patterns and the high-resolution images further suggest that the

cubic nanoprecipitates have cube-on-cube texture with the MgCNi_3 matrix. The absence of any mismatch strain fields in the high-resolution images and the fact that the precipitate lattice parameter is 25% larger than that of the matrix also indicates there is close to a five-on-four commensuration between the two phases. This explains why the cubic precipitates are not prominent in lower-magnification images.

To explain the unusual flux-pinning behavior, we note that the plot in Fig. 6 is strikingly similar to the behavior of optimized Nb 48 wt% Ti strands.¹² In that system, strong pinning is produced by a very fine two-phase nanostructure of 1–4-nm-thick α -Ti precipitates separated by 5–10 nm in a matrix of superconducting Nb-Ti. Since the (nonsuperconducting) precipitate thickness is a bit smaller than the flux-line core diameter $2\xi \approx 10$ nm at 4.2 K and since there is a higher number of precipitates than flux lines, individual core-pinning interactions can be summed up directly to give a pinning-force curve with a peak at $h \approx 0.5$. However, since just below $T_c = 9.1$ K the fluxon core becomes much larger due to the divergence of $\xi(T) \propto (1 - T/T_c)^{-1/2}$, the individual nanometer-scale α -Ti precipitates then become invisible to the flux lines and larger-scale precipitate clusters then become the pinning sites. This produces a pinning-force curve with a peak below $h = 0.25$ at 8.5 K. The lack of temperature scaling of $F_p(H)$ for Nb-Ti thus results from the combination of having nonsuperconducting regions distributed on a scale less than $\xi(0)$ and the diverging temperature dependence of ξ as $T \rightarrow T_c$.

In the present experiment, a similar distribution of precipitates that can act as pinning sites at length scales comparable to $\xi(0) \approx 5$ nm is present. Graphite is not a superconductor, which would give the necessary local suppression of superconductivity needed for flux pinning. Although we cannot identify the composition and exact structure of the cubic precipitates, band structure calculations^{3–5} suggest a strong sensitivity of superconductivity to the nickel atom bonds, including the possibility of ferromagnetic transitions. It is likely, therefore, that the cubic precipitates are also not superconducting. Moreover, while we cannot rule out a small level of excess pure nickel as the source of the ferromagnetic background, as discussed earlier, it is also possible that the cubic precipitates are ferromagnetic. As such, these would be especially potent pinning centers. We surmise, therefore, that the shift of the pinning force curve in Fig. 6 is the result of flux pinning by the nanoprecipitates at low temperature and its absence at T near T_c .

We do not believe collective pinning can account for this strong flux-pinning behavior. A clear signature of collective pinning in intergranular superconductors is the appearance of a peak effect near the irreversibility field, as described by Kes and Tsuei.²¹ This occurs when the critical current density is quite low. Adding pinning sites, e.g., by irradiation,²² results a crossover from this regime to the strong-pinning limit and the disappearance of the peak effect. Modern, optimized Nb_3Sn conductors never display a peak effect and have critical current densities well beyond this limit and in excess of 10^5 A/mm² at 12 T, 4.2 K.²³ The magnetization current density of 10^6 A/cm² is similar to the very high current densities found in Nb-Ti superconductors, which have $T_c = 9$ K

and $\mu_0 H_{c2}(0) \approx 16$ T and obey direct summation.¹² Based on the resistivity at T_c [$\rho = 120 \mu\Omega$ cm (Ref. 7)], the Sommerfeld coefficient of specific heat [$\gamma = 10$ mJ (molNi)⁻¹ K⁻² (Ref. 1)] and the slope of $\mu_0 H_{c2}(T)$ at the critical temperature given earlier, we estimate the Ginzburg-Landau parameter $\kappa = 66$ using the formalism of Ref. 20. This suggests that the pinning force per flux line $J_c \times \phi_0$ is of order 2×10^{-5} N/m, or about 10% of the flux-line tension $\mu_0 H_{c2}^2 \pi \xi^2 / 2 \kappa^2 \xi \approx 1.5 \times 10^{-4}$ N/m, where $\phi_0 = 2 \times 10^{-15}$ Wb is the flux quantum. This very strong pinning value lies well within the single-vortex pinning regime, where the flux-line lattice is plastically deformed.^{18,24}

Since direct summation is also implied by the shape of the pinning-force curves, the volume fraction of pinning sites must also be substantial¹² to provide a number of pinning sites inside each grain that is comparable to the number of flux lines threading through each grain. This is consistent with the large number of fringe domains in the moiré pattern images. A large fraction of precipitates should have a pronounced effect on the normal-state and superconducting properties. In particular, we observe a large slope $\mu_0 dH_{c2}/dT$ of -2.3 T/K at T_c , similar to the slope found in Ref. 7. This indicates that the excess-carbon processing technique used here results in a dirty-limit superconductor. These initial bulk samples of MgCNi₃ are thus more alike Nb-Ti alloys and (Nb,Ti,Ta)₃Sn compounds and unlike clean-limit RNi₂B₂C compounds.⁷ We speculate that pristine samples and single crystals of MgCNi₃, should they become available, might not exhibit such dirty-limit behavior and may instead be analogous to pure Nb and unalloyed Nb₃Sn.

On the other hand, if variants of the present MgCNi₃ bulk can be made with higher T_c while retaining the multiphase nanostructure, these may be technologically important. The present experiment shows that excellent flux-pinning properties are found together with high H_{c2} (relative to T_c). Of all the superconducting materials, perhaps only Nb-Ti alloys exhibit such a unique combination of pinning and high-field performance, and partly for this reason (ductility is the other) Nb-Ti alloys have been the mainstay of magnet technology since the 1960s. For example, the standard expression $H_{c2}(0) = 3110 \rho \gamma T_c$ (tesla) (Refs. 20 and 25) suggests upper critical fields of 20 T at low temperature could be obtained if T_c were doubled in a compound with comparable resistivity ρ and electronic specific heat coefficient γ to that found in MgCNi₃. In view of the fact that critical temperatures as high as 17 K have already been found in the nickel borocarbides [and 23 K in the similar compound YPd₂B₂C (Ref. 2)], further investigation of superconducting nickel-carbide intermetallics could be extremely valuable for magnet applications.

An interesting and perhaps very important result is the observation of single-flux-line pinning by intragranular pin-

ning sites in a polycrystalline intermetallic superconductor. This combination is extremely rare; generally grain-boundary pinning is dominant, and intermetallic superconductors exhibit characteristic bulk pinning-force curves that reach their peak at 20% of the irreversibility field, far below typical fields where they are applied. For example, Nb₃Sn superconductors attain their maximum value of F_p (at 4.2 K) at about 5 T, even though solenoid magnets made with Nb₃Sn now exceed operating fields of 20 T. To our knowledge, no other bulk intermetallic superconductor with fine grains exhibits the flux-pinning behavior shown in the present experiment. Previous reports have shown that pinning by, e.g., intragranular structural defects can take over when the grain size is very large²⁶ or when the flux lattice is very soft (the so-called “peak effect”²⁷). By analogy with the present experiment, artificially introducing a high number ($10^{15}/\text{m}^2$) of nanometer-scale intragranular pinning sites into intermetallic superconductors may produce more desirable pinning-force curve shapes and improve performance at high fields. This might be accomplished by implantation of ferromagnetic ions or heavy-ion irradiation.

IV. CONCLUSIONS

We have examined the flux-pinning properties and nanostructure of bulk polycrystalline MgCNi₃. The flux-pinning results are suggestive of a transition from pinning by grain boundaries at temperatures near T_c to core pinning by nanometer-scale intragranular precipitates at low temperatures. High-resolution transmission electron microscopy indicated the presence of both graphite and an unidentified cubic precipitate, with 5 nm size and substantial volume fraction. The precipitates may have formed because of processing with excess carbon. Since this has been the common method used to produce bulk samples, scattering due to a multiphase nanostructure may be the cause of dirty-limit behavior seen so far, and different behavior would be expected for single crystals and more pristine samples. The excellent flux-pinning properties observed may be unique among intermetallic superconductors, and ways to artificially produce an analogous nanostructure in other intermetallic superconductors were suggested. The presence of both high upper critical field and strong core pinning is a rare combination, suggesting that variants of MgCNi₃ with higher critical temperature and similar nanostructure may be technologically important.

ACKNOWLEDGMENTS

This work was supported by grants from the U.S. National Science Foundation and the U.S. Department of Energy. We would like to acknowledge helpful discussions with A. Polyanskii.

*Electronic address: ldcooley@facstaff.wisc.edu; www.asc.wisc.edu

¹T. He Q. Huang, A. P. Ramirez, Y. Wang, K. A. Regan, N. Rogado, M. A. Hayward, M. K. Haas, J. S. Slusky, K. Inumara,

H. W. Zandbergen, N. P. Ong, and R. J. Cava, *Nature* (London) **411**, 54 (2001).

²R. J. Cava, H. Takagi, B. Batlogg, H. W. Zandbergen, J. J. Krajewski, W. F. Peck, Jr., R. B. van Dover, R. J. Felder,

- R. Siegrist, K. Mizuhashi, J. O. Lee, H. Eisaki, S. A. Carter, and S. Uchida, *Nature (London)* **367**, 146 (1994); **367**, 252 (1994); T. Siegrist, H. W. Zandbergen, R. J. Cava, J. J. Krajewski, and W. F. Peck, Jr., *ibid.* **367**, 254 (1994).
- ³S. B. Dugdale and T. Jarlborg, *Phys. Rev. B* **64**, 100508(R) (2001).
- ⁴J. H. Shim, S. K. Kwon, and B. I. Min, *Phys. Rev. B* **64**, 180510 (2001).
- ⁵D. J. Singh and I. I. Mazin, *Phys. Rev. B* **64**, 140507(R) (2001).
- ⁶H. Rosner, R. Weht, M. D. Johannes, W. E. Pickett, and E. Tosatti, *Phys. Rev. Lett.* **88**, 027001 (2001).
- ⁷S. Y. Li, R. Fan, X. H. Chen, C. H. Wang, W. Q. Mo, K. Q. Ruan, Y. M. Xiong, X. G. Luo, H. T. Zhang, L. Li, Z. Sun, and L. Z. Cao, *Phys. Rev. B* **64**, 132505 (2001).
- ⁸M. D. Lan, J. C. Chang, K. T. Lu, C. Y. Lee, H. Y. Shih, and G. Y. Jeng, *IEEE Trans. Appl. Supercond.* **11**, 3607 (2001).
- ⁹J. S. Kouvel and J. B. Comly, *Phys. Rev. Lett.* **20**, 1237 (1968).
- ¹⁰M. Suenaga, A. K. Ghosh, Y. Xu, and D. O. Welch, *Phys. Rev. Lett.* **66**, 1777 (1991).
- ¹¹J. E. Evetts, *Concise Encyclopedia of Magnetic and Superconducting Materials* (Pergamon, New York, 1992), p. 99.
- ¹²C. Meingast and D. C. Larbalestier, *J. Appl. Phys.* **66**, 5971 (1989).
- ¹³W. A. Fietz and W. W. Webb, *Phys. Rev.* **178**, 657 (1969).
- ¹⁴D. P. Hampshire and H. Jones, *J. Phys. C* **20**, 3533 (1987); D. P. Hampshire, A. F. Clark, and H. Jones, *J. Appl. Phys.* **66**, 3160 (1989).
- ¹⁵A. Kahan, *Cryogenics* **30**, 678 (1991); *Phys. Rev. B* **43**, 2678 (1991).
- ¹⁶D. Dew-Hughes, *Philos. Mag. B* **55**, 459 (1987).
- ¹⁷J. R. Clem, in *Low Temperature Physics—LT-13*, edited by K. D. Timmerhaus, W. J. O'Sullivan, and E. F. Hammel (Plenum, New York, 1974), p. 102.
- ¹⁸A. M. Campbell and J. E. Evetts, *Adv. Phys.* **21**, 199 (1972).
- ¹⁹W. Kesternich, *Materials Problem Solving with the Transmission Electron Microscope*, edited by L. W. Hobbs, K. H. Westmacott, and D. B. Williams, *Mater. Res. Soc. Symp. Proc. No. 62* (Materials Research Society, Pittsburgh, 1986), p. 229.
- ²⁰T. P. Orlando, E. J. McNiff, Jr., S. Foner, and M. R. Beasley, *Phys. Rev. B* **19**, 4545 (1979).
- ²¹P. H. Kes and C. C. Tsuei, *Phys. Rev. Lett.* **47**, 1930 (1981).
- ²²R. Meier-Hirmer, H. K pfer, and H. Scheurer, *Phys. Rev. B* **31**, 183 (1985).
- ²³T. Pyon and E. Gregory, *IEEE Trans. Appl. Supercond.* **11**, 3688 (2001); M. Field, R. Hentgens, J. Parrell, Y. Zhang, and S. Hong, *ibid.* **11**, 3692 (2001).
- ²⁴G. Blatter, M. V. Feigel'man, V. B. Geshkenbein, A. I. Larkin, and V. M. Vinokur, *Rev. Mod. Phys.* **66**, 1125 (1996).
- ²⁵B. B. Goodman, *Rep. Prog. Phys.* **49**, 445 (1966).
- ²⁶L. A. Bonney, T. C. Willis, and D. C. Larbalestier, *J. Appl. Phys.* **77**, 6377 (1995).
- ²⁷R. Wordenweber, P. H. Kes, and C. C. Tsuei, *Phys. Rev. B* **33**, 3172 (1986).